Applied Mathematical Modelling 35 (2011) 1591–1602

Contents lists available at ScienceDirect

Applied Mathematical Modelling

journal homepage: www.elsevier.com/locate/apm

Validation of LES predictions for turbulent flow in a Confined Impinging Jets Reactor

Matteo Icardi [a,*], Emmanuela Gavi [b], Daniele L. Marchisio [a], Michael G. Olsen [c], Rodney O. Fox [b], Djamel Lakehal [d]

[a] Dip. Scienza dei Materiali e Ingegneria Chimica, Politecnico di Torino, C.so Duca degli Abruzzi 24, 10129 Torino, Italy
[b] Department of Chemical and Biological Engineering, Iowa State University, 3162B Sweeney Hall, Ames, IA 50011-2230, USA
[c] Department of Mechanical Engineering, Iowa State University, 3025 Black Engineering Building, Ames, IA 50011-2230, USA
[d] ASCOMP GmbH, Technoparkstrasse 1, CH-8005 Zurich, Switzerland

ARTICLE INFO

Article history:
Received 2 September 2010
Accepted 20 September 2010
Available online 29 September 2010

Keywords:
Micro-mixer
Confined Impinging Jets Reactor
Large Eddy Simulation
Immersed Surfaces Technique

ABSTRACT

This work focuses on the prediction of the turbulent flow in a three-dimensionial Confined Impinging Jets Reactor with a cylindrical reaction chamber by using Large Eddy Simulation. Three-dimensional unsteady simulations with different sub-grid scale models, numerical schemes and boundary conditions were performed for various flow rates, covering different flow regimes. First, a qualitative analysis of the flow field was carried out and then predictions of the mean and fluctuating velocities were compared with micro Particle Image Velocimetry data. Good agreement was found both for the mean velocity components and the fluctuations. For low to moderate Reynolds numbers the sub-grid scale model was found not to be very relevant, since small scales are of less importance, as long as scalar transport and chemical reaction are not in play. An important finding is the good prediction of the high velocity fluctuations detected in particular at higher Reynolds number due to the natural instability of the system, strongly enforced by the jets unsteadiness.

1. Introduction

In many chemical/process engineering fields (e.g., pharmaceutical, cosmetics, pesticides, etc.) there is a strong interest in micro- and nano-particles [1–9]. These particles are generally produced via precipitation processes in particular types of passive mixers, such as the Confined Impinging Jets Reactor (CIJR) [10] or the multi-inlet vortex reactor [11–14]. CIJRs are indeed widely used nowadays and are preferred over other geometries due to their high mixing efficiency. In all these processes it is very important to control the properties of the particles, namely their Particle Size Distribution (PSD), shape and morphology, as well as composition [15–18]. The PSD is indeed strongly dependent on the mixing rate, and very fine particles with very narrow distributions are obtained only under extremely efficient mixing conditions. The design, optimisation and scale-up of these devices can be efficiently investigated through computational fluid dynamics (CFD). However, the simulation of the flow field and mixing dynamics is often complicated by the fact that, under typical operating conditions and due to their small geometry, the flow is usually in the transitional regime. The first important step of the CFD analysis is to obtain a deep understanding of the flow field and turbulent phenomena inside the reactors which strongly influence the chemical reac-

* Corresponding author. Tel.: +39 0115644695; fax: +39 0115644699.
E-mail address: matteo.icardi@polito.it (M. Icardi).

0307-904X/$ - see front matter © 2010 Elsevier Inc. All rights reserved.
doi:10.1016/j.apm.2010.09.035

tions, particles formation and their interactions. In this type of reactors, the particles have a very small size, a density very similar to the fluid (i.e., water) and they are very dilute, so that they usually have a negligible influence on the final flow and turbulent fields. Generally the results of single-phase simulations can be extended to the multi-phase real system. For these reasons the results of this work are limited to the non-reactive single-phase case, which can be compared to experimental μPIV data, obtained with a single fluid without reactions.

Many studies on the flow field in these devices and reactors have been carried out with steady-state Reynolds-Average-Navier–Stokes (RANS) simulations [19,20,13,16] with different turbulence models. This approach is computationally efficient and it can result in reasonably good agreement with experimental data; however it cannot capture the truly unsteady behaviour of the flow that could be very important, especially when chemical reactions are considered. In these cases this approach has to be abandoned and other more sophisticated techniques, such as Direct Numerical Simulation (DNS) and Large Eddy Simulation (LES) should be adopted instead.

DNS can be used, for example, in order to obtain reliable and detailed data on these systems [21,22]. In this case, in fact, no approximation is made in the computational model and the governing Navier–Stokes equations are directly solved, therefore they can be considered as virtual experiments and used to develop RANS and LES closures. DNS is widely used for flows characterised by low and moderate Reynolds numbers and can be employed for both theoretical and applied research. However, since it could be very expensive in terms of simulation times, especially when it comes to the description of realistic geometries and flow conditions, it cannot be employed in many industrial and practical applications. Another important limitation of DNS becomes apparent when scalar concentrations have to be calculated for a liquid in the turbulent regime. In this case the smallest length scales of fluctuations in scalar concentrations (i.e., the Batchelor scale) can be much smaller than the Kolmogorov scale (i.e., the smallest scales of velocity fluctuations) [23] and grids that can resolve the Batchelor scale are still intractable from a practical point of view. For these reasons the research on turbulence models is still an open and interesting issue, especially when applied to turbulent reactive flows. It is in this spirit that the present work has been undertaken.

An interesting alternative to DNS is LES [24,14,25]. With this approach, only the larger scales, containing most of the energy and responsible for the main transport properties, are solved with an appropriate sub-grid scale (SGS) model. These simulations can be also very expensive compared to RANS (although less expensinve than DNS) because they are inherently time-dependent and three-dimensional, but they have recently become very attractive due to increased computing capabilities. It is however worth noting that our previous work on turbulence in the CIJR [24] demonstrates that the higher accuracy and characteristic of LES models does not always translate in better predictions for the flow field and the chemical reactions. This is because while in the RANS approach only the mean values are important, and the fluctuations are implicitly taken into account in the turbulence model, in LES an unsteady and more detailed model is used that must be provided with accurate and realistic boundary conditions.

In this work LES of the flow field in a CIJR for a single-phase non-reactive test-case is validated against experimental measurements. The experiments on the CIJR used here for model validation [24,22] were obtained with the micro Particle Image Velocimetry (μPIV) technique. μPIV is an extension of Particle Image Velocimetry (PIV) developed to study micro-devices [26,27]. In a typical μPIV system [28], the microfluidic device of interest is imaged using an inverted fluorescence microscope. Fluorescent seed particles are illuminated by a double-pulsed Nd:YAG laser and the emitted light from the particles is imaged onto a CCD camera. The images are analysed using a cross-correlation technique and an instantaneous velocity vector field is obtained. For more details about μPIV the reader is referred to a recent review [29]. It is important to highlight here that these measurements are conducted in a three-dimensional device in a turbulent regime. These conditions make the experimental setup extremely difficult and results cannot be simply filtered to neglect spurious fluctuations caused by experimental errors. DNS carried out on the very same system [22] demonstrates that detailed boundary conditions are crucial to simulate the real experimental behaviour and an accurate approximation was proposed. Starting from these results, the objective of this work is to build and validate a LES tool to predict the fluid dynamics in the CIJR to avoid the use of expensive DNS. This will be of particular importance in a later stage of this work when computational models for scalar transport, chemical reactions and particles formation will be added.

The manuscript is organised as follows. Firstly the theoretical background and concepts of turbulent flow simulation and numerical methods are presented, followed by a description of the operating and boundary conditions. The results are then discussed and compared with the available experimental data. Finally some conclusions are drawn and future steps are envisioned.

2. Model description

2.1. Fluid flow equations

The single phase flow inside the CIJR is investigated in this work by solving the incompressible Navier–Stokes equations.

Although the inflow conditions are laminar, the jet impingement creates strong flow instabilities and spatial variations that lead to turbulence (i.e., flow containing a wide range of time- and length-scales), and when the computational grid is not fine enough to resolve all the scales arising from the interaction of the jets, a model is required to represent their effect on the macro-scale flow.

The governing equations are solved, either within the RANS framework, in which flow variables are decomposed into an average and a fluctuating term, and only the average field is described, or in a filtered form (LES), where flow variables appear as filtered quantities. In the LES framework, the filtered velocity for example becomes [30]

$$\overline{\mathbf{U}}(\mathbf{x},t) = \int G(\mathbf{r}-\mathbf{x})\mathbf{U}(\mathbf{r},t)d\mathbf{r}, \tag{1}$$

where G is the filter function. The most common filter is the so-called "box filter", which directly makes use of the finite-volume approximation of the spatial operators. The application of Eq. (1) to the momentum equation results in a closure problem, namely the residual stress tensor [30]

$$\tau_{ij}^r = \overline{U_iU_j} - \overline{U_i}\,\overline{U_j} - \frac{1}{3}(\overline{U_iU_i} - \overline{U_i}\,\overline{U_i}), \tag{2}$$

that needs to be modelled in terms of macro-scale flow variables by using a SGS model.

The simplest SGS model is the so-called "constant Smagorinsky" model [31] in which the residual stress terms are modelled as

$$\tau_{ij}^r = -2(C_S\Delta)^2|\overline{S}|\overline{S}_{ij}, \tag{3}$$

where Δ is the bandwidth of the filter, $\overline{S}_{ij}$ is the filtered strain rate, $|\overline{S}|$ is its norm and C_S is the Smagorinsky constant. Other SGS models have been developed, and one of the most popular is the dynamic model of Germano [32], proposed to dynamically predict a wider range of flow regimes, from transitional to "fully developed" turbulence.

2.2. Numerical methods

Computations are carried out with the commercial CFD code *TransAT* [33]. The equations are solved with a finite-volume approximation and solid boundaries are represented with the Immersed Surfaces Technique (IST) [33]. In this numerical technique, similar to the immersed boundary methods [34], the grid cells intersects the solid walls without fitting to them. To impose the non-slip condition, instead of using a penalty approach, it makes use of an implicit representation of the walls by defining of a level set function (ϕ_s). It is a signed distance function positive in the solid phase and negative in the fluid phase and null on the fluid–solid interface. The equations in the solid and fluid domain are combined using a smoothed Heaviside function:

$$\mathrm{H}(\phi_s) = \frac{1}{2}\left(1 - \tanh\left(\frac{2\phi_s}{\delta_{sf}}\right)\right), \tag{4}$$

which varies between one (in the fluid phase) and zero (in the solid phase) and takes intermediate values in the fluid–solid finite interface of thickness δ_{sf}. The final density ρ and velocity U_i can be formally defined as

$$\rho = H\rho^f + (1-H)\rho^s, \tag{5}$$

$$\rho U_i = H\rho^f U_i^f + (1-H)\rho^s U_i^s, \tag{6}$$

where U_i^f and ρ^f are respectively the fluid velocity and density and U_i^s and ρ^s are the corresponding values for the solid.

For the solid phase the following equations are solved [33]:

$$\frac{\partial\rho^s}{\partial t} + \frac{\partial}{\partial x_j}\left(\rho^s U_j^s\right) = 0, \tag{7}$$

$$\frac{\partial}{\partial t}\left(\rho^s U_i^s\right) + \frac{\partial}{\partial x_j}\left(\rho^s U_i^s U_j^s\right) = 0. \tag{8}$$

For the case of non-moving immersed surfaces, the solid phase velocity is set equal to zero ($U_i^s = 0$) whereas the standard Navier–Stokes equations are solved for the fluid phase:

$$\frac{\partial\rho^f}{\partial t} + \frac{\partial}{\partial x_j}\left(\rho^f U_j^f\right) = 0, \tag{9}$$

$$\frac{\partial\rho^f U_i^f}{\partial t} + \frac{\partial}{\partial x_j}\left(\rho^f U_i^f U_j^f\right) = -\frac{\partial p^f}{\partial x_i} + \frac{\partial}{\partial x_j}\left(2\mu^f S_{ij}^f\right), \tag{10}$$

where S_{ij}^f is the stress tensor and μ^f is the fluid viscosity. Summing up the equations of the solid and liquid phase, multiplied by his respective Heaviside functions and using Eq. (5), the following equations are obtained:

$$\frac{\partial\rho}{\partial t} + \frac{\partial}{\partial x_j}(\rho U_j) = 0, \tag{11}$$

$$\frac{\partial\rho U_i}{\partial t} + \frac{\partial}{\partial x_j}\left(\rho U_i U_j\right) = -\mathrm{H}(\phi_s)\frac{\partial p^f}{\partial x_i} + \frac{\partial}{\partial x_j}(2\mu S_{ij}) - 2\mu^f S_{ij}^f n_j\delta(\phi_s). \tag{12}$$

The last term in the RHS is a viscous shear stress at the interface (i.e., the solid wall), where n_j is the normal to the fluid–solid interface and $\delta(\phi_s)$ is the Dirac delta function representing the location of the interface. The wall shear itself is modelled as [35],

$$2\mu^f S_{ij}^f n_j = 2\mu^f \left(\frac{\rho}{\rho^f}\right) \frac{U_i}{H} \delta(\phi_s). \tag{13}$$

Since the walls are immersed in a cartesian grid, meshing time is considerably reduced and the accuracy of the numerical scheme can be preserved since the grid-skewness induced diffusion is simply eliminated. These two elements make the IST approach very useful to simulate unsteady turbulent flows in complex geometries.

The pressure–velocity coupling is performed by using the SIMPLEC algorithm [36]. Time discretization is performed with a third order explicit Runge–Kutta scheme. The advective terms are discretised with the HLPA scheme [37], which combines a second-order upstream-weighted approximation with the first-order upwind differencing under the control of a convection boundedness criterion. This scheme assures good convergence and stability properties but was demonstrated to be not the most suitable for DNS and LES [38] where the algorithms must be accurate enough to avoid numerical viscosity/diffusion [36], which represents an additional viscosity "artificially introduced" by discretization errors. For this reason simulations with the QUICK scheme [39] were also performed.

Two SGS models are used: the Smagorinsky model with a model constant $C_S = 0.08$, to limit diffusion in the near-wall region and the dynamic Germano model in its standard formulation. In the wall flow-regions, the Werner–Wengle wall functions [40] are used, together with the van Driest damping function [41].

3. Operating and boundary conditions

Fig. 1 represents the meridian section of the three-dimensional geometry of the CIJR used both for simulations and experiments. It consists of a cylindrical reaction chamber and rounded inlet and outlet tubes. The flow enter the reactor through two opposing tubes of diameter $d_j = 1$ mm with a mean velocity u_j, and then exit through the lower tube of diameter $2d_j = 2$ mm. The diameter of the reactor is $D = 4.8$ mm and the total volume of the chamber is approximately $V = 1.73 \times 10^{-7}$ m^3 resulting in very short mean residence times. The flow regime in the reactor can be generally characterised by the jet Reynolds number, based on the inlet jet diameter and the average inflow velocity as

$$Re_j = \frac{u_j d_j \rho^f}{\mu^f}. \tag{14}$$

Fluid properties are selected by reference to the experiments, which employed an aqueous solution of urea with a density $\rho^f = 1.141$ g/cm^3 and a viscosity $\mu^f = 1.914$ cPs (this fluid was selected due to its index of refraction which more closely matched the index of refraction of the reactor walls). Five different flow rates were investigated in this work and inlet con-

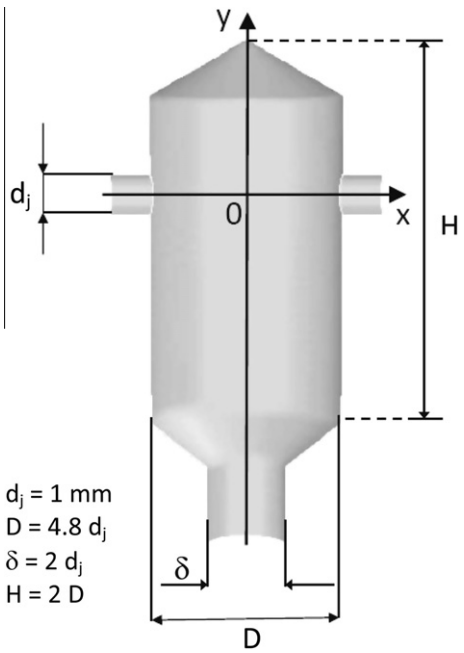

Fig. 1. Schematic geometry of the CIJR under study.

Table 1
Nominal flow rates, measured mean velocities, mean residence times and jet Reynolds numbers.

FR (mL/min)	u_j (m/s)	τ_R (s)	Re_j
10	0.105	1.05	62
20	0.25	0.44	150
40	0.52	0.21	310
90	1.01	0.11	600
150	1.5	0.074	900

Table 2
Computational grids used for simulations: Grid number, number of internal cells used for computing the flow and cell size.

	Cells	Internal cells	Δx (μm)
1	$40 \times 40 \times 80$	1×10^5	100–140
2	$68 \times 60 \times 128$	3.5×10^5	50–80
3	$100 \times 84 \times 150$	8.5×10^5	30–60

ditions are reported together with the mean residence time and the jet Reynolds number in Table 1. The Reynolds numbers calculated using the inlet diameters and the mean velocities show that the flow regime in the inlet tubes is laminar, thus parabolic velocity profiles have been imposed. Experimental data are available only for the first four Flow Rates

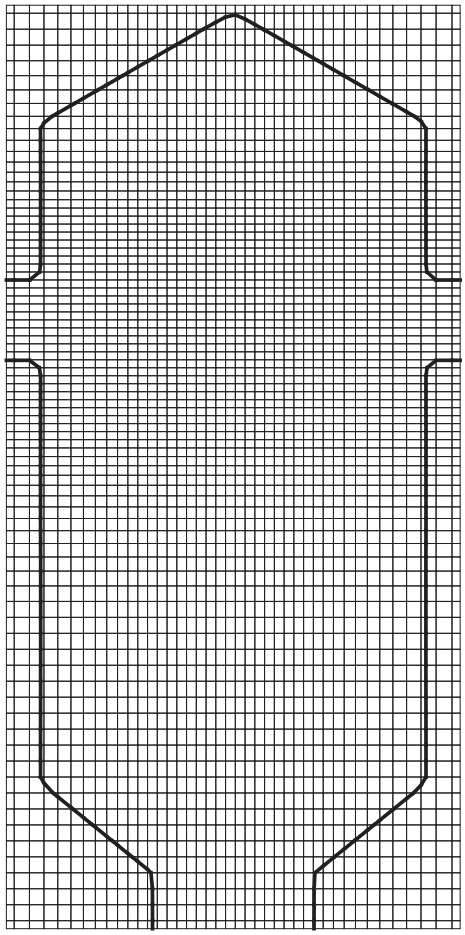

Fig. 2. The grid used for LES.

(FR = 10,20,40,90 mL/min) and the additional case (FR = 150 mL/min) was included to investigate the effects of numerical schemes and SGS models at higher Reynolds numbers. Due to the unavoidable experimental inaccuracies, these flow rates do not correspond exactly to the velocities observed in the inlets, therefore we refer to them as "nominal flow rates".

In our previous work [22] it has been demonstrated that in the simulations the constant laminar inflows must be modified, superposing a small oscillation proportional to the laminar profile. This was due to the impossibility of maintaining purely steady velocities at the reactor inlets in the experiments. This unsteadiness at the reactor inlets is due to a number of factors, including inherent pump unsteadiness and varying pressure within the reactor due to the unsteady motion of the impingement zone feeding back to cause unsteady inlet flow conditions. Therefore in the present simulations the same oscillating inflows, solely determined by the experimental data, are imposed by using a single harmonic oscillation in both the inflows. They are set to be in phase opposition in order to emphasise the effects of unsteady asymmetric flows. The oscillation was set proportional to the original parabolic profile (to avoid a negative inflow velocity) with amplitude equal to one tenth of the constant velocity to fit the standard deviation obtained in the experiments with FR = 10 mL/min, which is the case where the external instabilities are more evident.

Simulations were performed on a Linux workstation (4 $\times$ Intel (R) Xeon (R) CPU 5160 3.00 GHz) with shared memory parallelism (Open-MP library). Using four processors the speed-up factor was found to be between 2 and 2.5 and approximately one or two days of CPU time were needed to simulate six residence times depending on the FR investigated.

An initial set of simulations was carried out with three different non-uniform Cartesian grids with a total factor of refinement between the smallest and the biggest cell equal to two. The number of total and internal cells (i.e., the grid actually used in the IST context to compute the flow) and the minimum cell size of the different grids are reported in Table 2. Dimensional analysis and grid sensitivity studies revealed that grid 1 can resolve most of the energy-containing scales. In fact the results for this grid in terms of mean and fluctuating velocity are almost equal to the results obtained with grid 2 and grid 3. In particular if FR < 40 mL/min, most of the involved scales are resolved and the LES can almost be considered as a DNS. In this case in fact the SGS viscosity is very low and the flow is not fully turbulent. At the higher FR values investigated instead, the SGS model becomes more important. The results reported in this work were obtained with grid 1 and a meridian section of the grid is displayed in Fig. 2.

Results were compared in the same window captured by μPIV and simulations data were saved and analysed at each time step after that the influence of initial conditions disappeared (i.e., three mean residence times) for a time interval equivalent to three mean residence times for the two lowest FR. For the two highest FR when the flow is more chaotic, the time interval length was chosen longer (six mean residence times) to obtain more accurate statistics. Time steps were chosen adaptively according to convergence conditions and resulted approximately in 10^4 time steps for each mean residence time. The spatial resolution in μPIV is defined by the dimensions of the interrogation volume. In the present experiments, the in-plane velocity vector spacing in the PIV measurements was 140 μm, and the out-of-plane dimension of the measurement volume, defined as the depth of correlation [42,43], was 47 μm. For comparison, the grid cell size in the Large Eddy Simulations was approximately 100 μm in the region investigated.

4. Results and discussion

As already reported, simulations are statistically analysed only after transient effects decay, so that the influence of the initial condition has disappeared. First snapshots of the instantaneous flow field from the simulations with FR = 90 mL/min are reported to emphasise the importance of imposing the proper boundary conditions. Then detailed comparisons of the mean velocity U_x^{MEAN} along the x-axis, mean velocity U_y^{MEAN} along the y-axis and the root mean square (RMS) of fluctuating velocities $U_x'^{RMS}$ and $U_y'^{RMS}$ are analysed for each FR with different SGS models and numerical schemes.

4.1. Instantaneous flow field

Figs. 3 and 4 show two instantaneous velocity magnitude fields with FR = 90 mL/min obtained with different inflow conditions. On the left the simulation is performed by using constant inlet flow rates equal to the nominal one. As it is seen, a quasi-steady behaviour with large-scale fluctuations is observed. On the right the results obtained with the more realistic oscillating inlet flow rates, mimicking the experimental conditions, as shown in DNS in our previous work [22], are shown. As it is possible to see the variable asymmetric inflow conditions drastically change the flow behaviour, developing more scales, which are not created with constant inflows, even after refining the grid. These different scales are clearly identifiable when looking at the vorticity magnitude reported in Fig. 5. Vorticity is a good indicator of the flow structures and scales created and dissipated and their interaction with the local shear. The image on the left, taken from the constant inflow simulation, shows the onset of large structures created at impingement. The image on the right, taken from the variable inflows simulation, reveal the existence of smaller scales, generated from the breakup of the larger ones, responsible for the dissipation mechanism of turbulence. As will be highlighted later, this process of creation/destruction of flow scales followed by small-scale vorticity generation is very important to guarantee good mixing conditions. This analysis shows the importance of using accurate boundary conditions. As already mentioned, our previous work (based on comparison between DNS and μPIV) showed that only by employing these boundary conditions with small oscillations, good agreement with experimental data is obtained. Therefore in what follows only results obtained with oscillating inflows are reported.

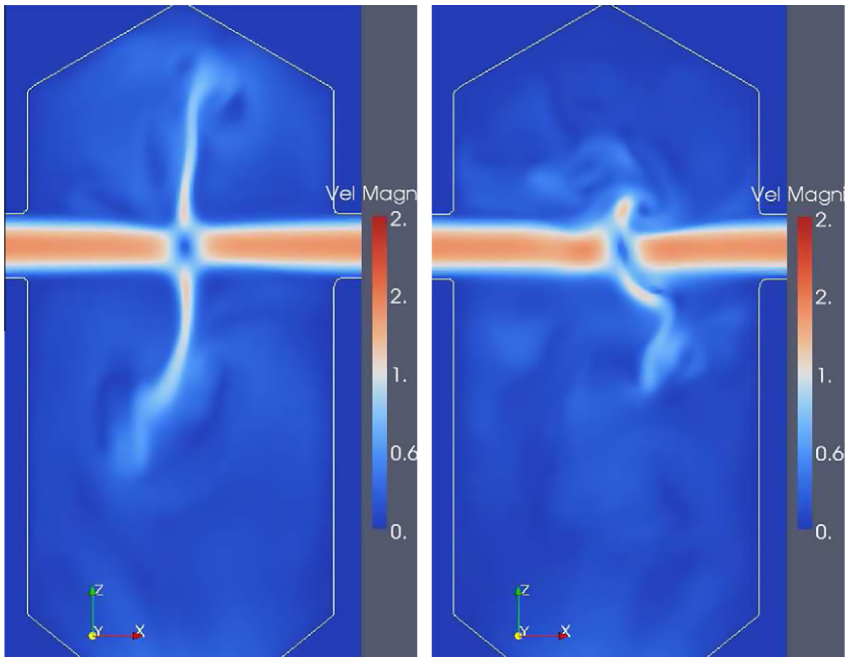

Fig. 3. Instantaneous velocity magnitudes with FR = 90 mL/min and constant symmetric inflows ($\Delta t = 0.1$).

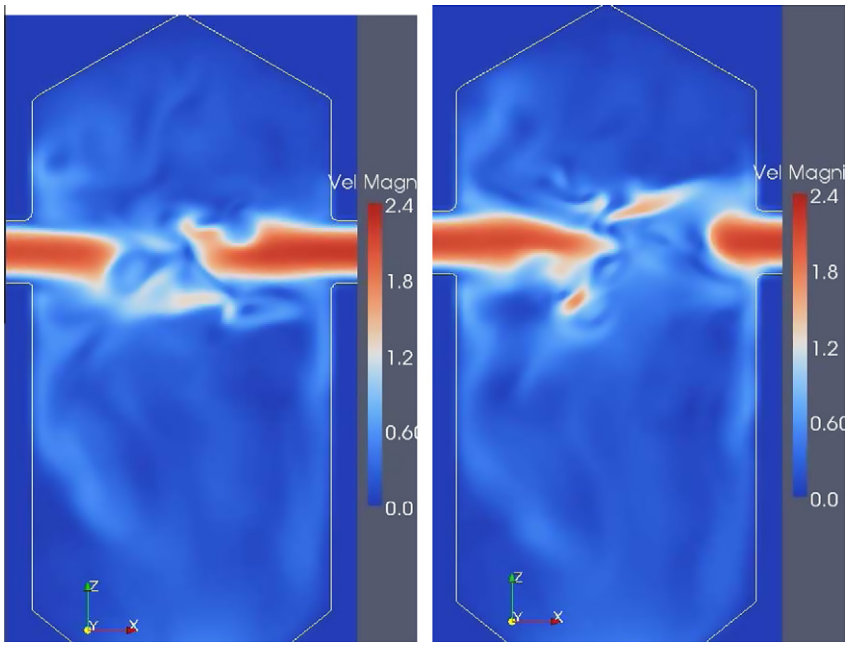

Fig. 4. Instantaneous velocity magnitudes with FR = 90 mL/min and constant symmetric inflows ($\Delta t = 0.1$).

4.2. Flow statistics

The comparison with experiments can be carried out by analysing the statistics of the flow along the inlet and outlet axes near the impinging point. This is in fact the region where the most important phenomena occur. Fig. 6 shows the mean x- and y-velocity components and the root-mean-square (RMS) of fluctuations along the x and y directions. LES predictions obtained with the constant SGS model together with the HLPA scheme (continuous line) are compared with the predictions obtained with constant Smagorinsky with the QUICK scheme (dashed line) and with predictions obtained with the dynamic

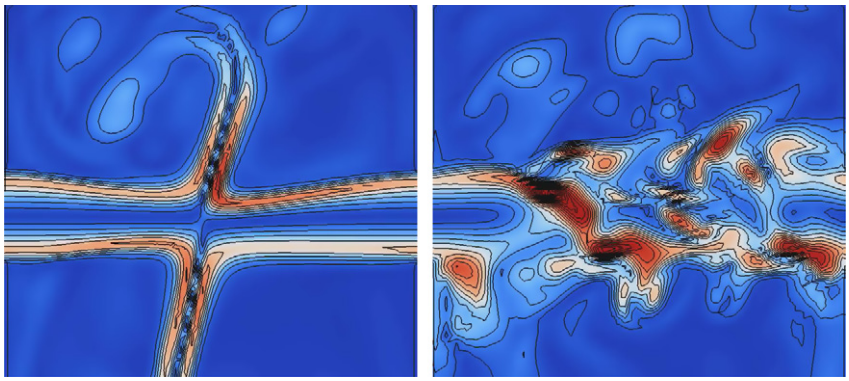

Fig. 5. Details of instantaneous vorticity magnitudes in the centre of the reactor with FR = 90 mL/min: comparison between constant inflows (left) and unsteady asymmetric inflows (right).

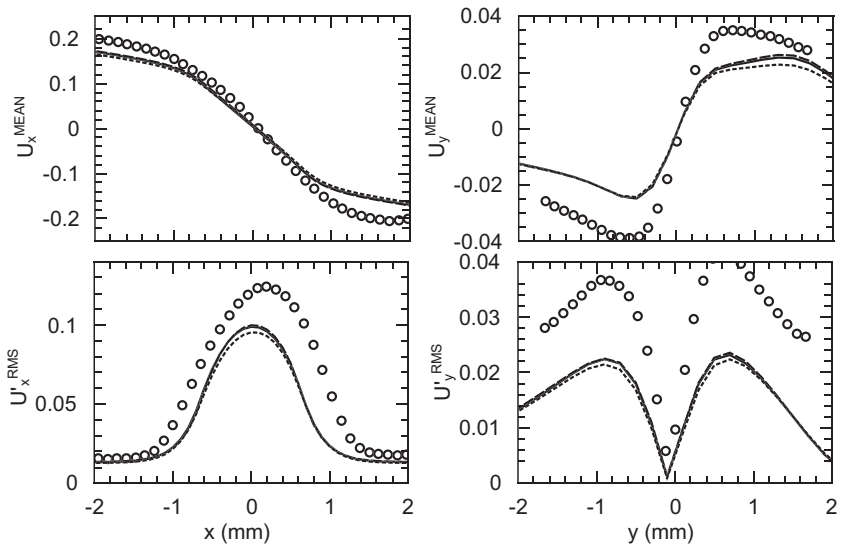

Fig. 6. Flow statistics with FR = 10 mL/min: Comparison between μPIV experiments (symbols), LES with HLPA scheme and constant SGS model (continuous line), LES with QUICK scheme and constant SGS model (dashed line), LES with HLPA scheme and dynamic SGS model (dotted line). From left to right and top to bottom: mean x-velocity along the x-axis at $y = 0$ mm, mean y-velocity along the y-axis at $x = 0$ mm, RMS of x-velocity fluctuations along the x-axis at $y = 0$ mm, RMS of y-velocity fluctuations along the y-axis at $x = 0$ mm.

SGS model by Germano with the HLPA scheme (dotted line). No significant differences were observed within the three modelling and numerical options because at this FR the flow is quite uniform. However, as can be observed by comparing simulations with experimental results (represented with open symbols), LES is capable to approximate both first order (i.e., mean velocities) and the second order (i.e., RMS of velocity fluctuations) statistics.

An increase in the inflow velocity triggers the onset of a more unsteady flow regime and a weakly turbulent behaviour can be observed. In particular with intermediate flow rates (FR = 20–40 mL/min) the flow starts to naturally oscillate but the amplitude and positions of oscillations would not be captured if constant boundary conditions were used. These operating conditions result in a transitional regime (between laminar and turbulent). The energy-containing cascade is not fully developed and this results in less accurate predictions.

In Fig. 7, predictions are compared to experiments for FR = 20 mL/min. Although x-fluctuations are overestimated, causing big fluctuations of the impingement plane and therefore smaller mean y-velocity at $x = 0$, the overall behaviour of the system is decently predicted. At this FR the difference between HLPA and QUICK schemes seems to be more evident in the propagation of oscillations along the x-direction, that the latter one seems to preserve, diffusing less than the former.

It should be mentioned that for FR values greater than 40 mL/min, the experimental uncertainties starts to become more and more important. This is partially related to the curved shape of the reactor walls as well as the small dimension of the device that make it very difficult to perfectly centre the observation plane. For example, one side of the piece of Plexiglas in

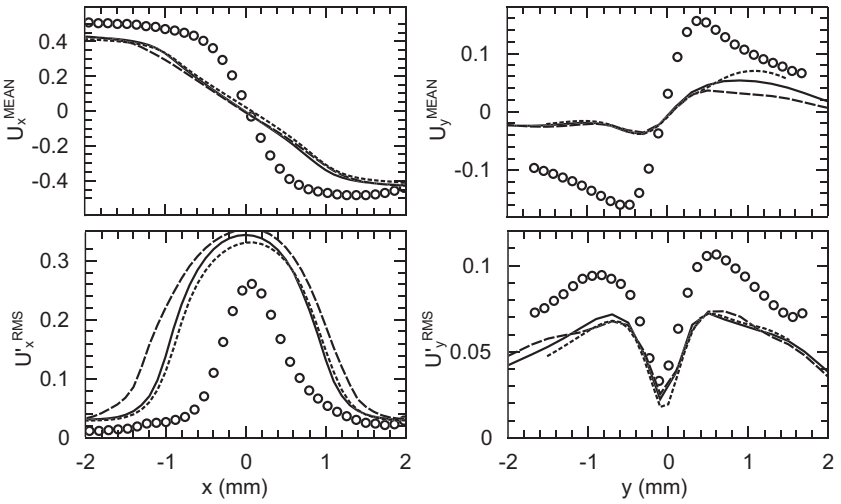

Fig. 7. Flow statistics with FR = 20 mL/min: Comparison between μPIV experiments (symbols), LES with HLPA scheme and constant SGS model (continuous line), LES with QUICK scheme and constant SGS model (dashed line), LES with HLPA scheme and dynamic SGS model (dotted line). From left to right and top to bottom: mean x-velocity along the x-axis at $y = 0$ mm, mean y-velocity along the y-axis at $x = 0$ mm, RMS of x-velocity fluctuations along the x-axis at $y = 0$ mm, RMS of y-velocity fluctuations along the y-axis at $x = 0$ mm.

which the reactor chamber is embedded is machined flat to rest on the microscope stage. Any misalignment of this machined side with the centre plane of the reactor where the inlet jets impinge will cause some discrepancies when the data are compared with centre-plane simulation data. Moreover, as the FR is increased, it becomes more difficult for the pumps to guarantee perfectly constant and balanced flow rates. As a matter of fact, although the experimental data were obtained with state of the art equipments and carefully selected operating conditions, some asymmetry and misalignement in the experimental profiles are still detectable (see Figs. 8 and 9). For example, the stagnation point is no more centred in the chamber therefore the y-velocity profiles are also misaligned. More details on the experimental work can be found in [24].

In Fig. 8 comparisons for FR = 40 mL/min are reported. As can be seen, also in this case (as for FR = 20 mL/min) the RMS is slightly overpredicted, whereas the predictions for the mean velocities result in better agreement with experiments. This could be due to the approximation of the fluctuating boundary conditions that emphasises the collision instability. The

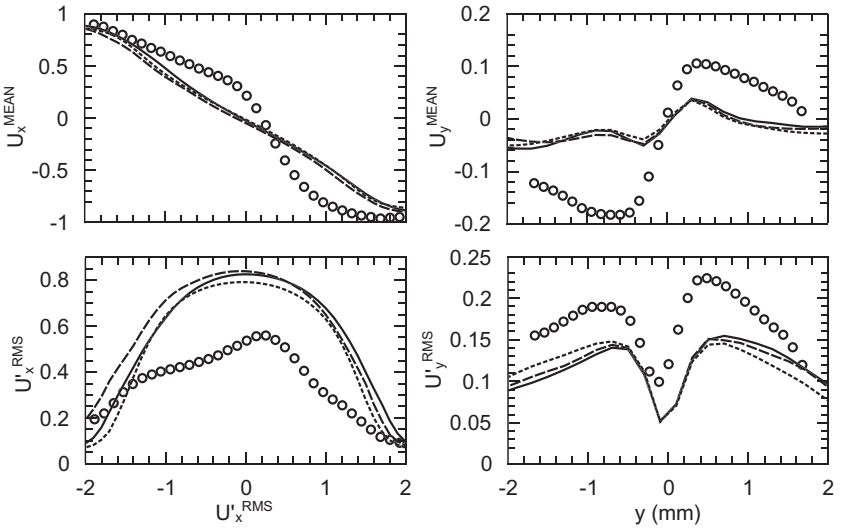

Fig. 8. Flow statistics with FR = 40 mL/min: Comparison between μPIV experiments (symbols), LES with HLPA scheme and constant SGS model (continuous line), LES with QUICK scheme and constant SGS model (dashed line), LES with HLPA scheme and dynamic SGS model (dotted line). From left to right and top to bottom: mean x-velocity along the x-axis at $y = 0$ mm, mean y-velocity along the y-axis at $x = 0$ mm, RMS of x-velocity fluctuations along the x-axis at $y = 0$ mm, RMS of y-velocity fluctuations along the y-axis at $x = 0$ mm.

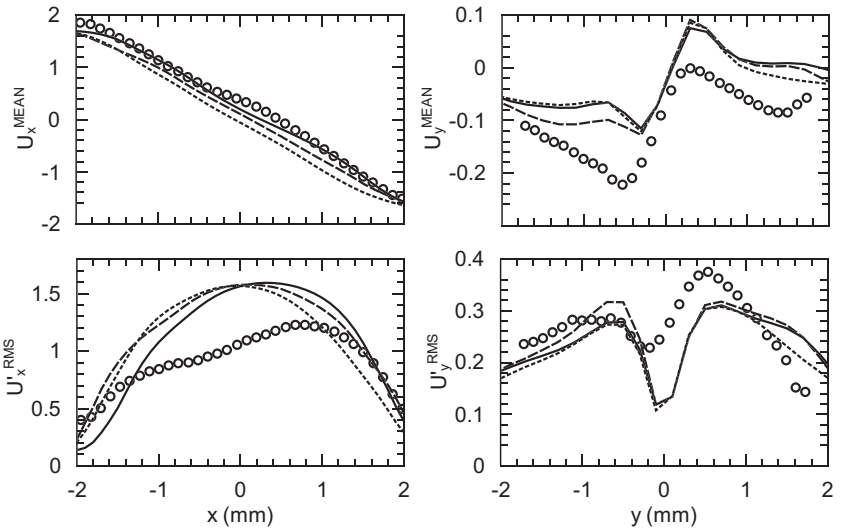

Fig. 9. Flow statistics with FR = 90 mL/min: Comparison between μPIV experiments (symbols), LES with HLPA scheme and constant SGS model (continuous line), LES with QUICK scheme and constant SGS model (dashed line), LES with HLPA scheme and dynamic SGS model (dotted line). From left to right and top to bottom: mean x-velocity along the x-axis at $y = 0$ mm, mean y-velocity along the y-axis at $x = 0$ mm, RMS of x-velocity fluctuations along the x-axis at $y = 0$ mm, RMS of y-velocity fluctuations along the y-axis at $x = 0$ mm.

agreement, both for first and second order statistics, significantly improves for the last case for which experimental data are available. The case for FR = 90 mL/min approaches "fully turbulent" behaviour and LES can accurately predict the smooth x-velocity profile and the relatively high fluctuations along the entire x-axis. Also the predictions for the y-velocity component (both mean value and RMS of fluctuations) result in very good agreement with experimental data. However it should be remembered here that the experiments reveal a shifted position of the impingement point that is not predictable in the simulations where symmetric inflows were imposed. In fact, the impingement point can be recognised (at least by null mean velocities) even if it moves chaotically in the chamber. This shifting is further confirmed in the y-velocity experimental profiles that, for this reason, do not represent exactly the plane where the jets collide.

For high FR the y-velocity profiles are indeed very sensitive to the jets alignment, symmetry and oscillations because the y-velocity is everywhere small compared to the x-component except at the impingement point where it can be relatively large. So the y-velocity profiles are not always well predicted because the impingement fluctuations are slightly overpredicted in the simulations (as shown in x-velocity fluctuations) and the y-fluctuations result to be more distributed along the x-axis instead of being more concentrated at the measurement position $x = 0$. However this effect do not have a strong influence the overall turbulence and mixing efficiency in the reactor.

As a general comment it is possible to state that the comparison with experimental data showed little influence of the numerical scheme adopted. In fact, for the operating conditions investigated in this work, predictions obtained with HLPA were found to be very close to those obtained with QUICK. This could be a consequence of the very regular grid used in this work, that are already characterised by a small numerical diffusion, notwithstanding the numerical scheme adopted. The effect of the SGS seems to be slightly more important, although no significant difference is detected, proving probably that for the geometry and the operating conditions investigated the constant Smagorinsky model is adequate.

Moreover, as already reported, for the considered flow regimes the turbulent behaviour of the system is not only due to the impingement of the jets, which induces a strong unsteady behaviour limited to a small region in the centre of the reactor, but also to the non-constant inlet flow rates. This suggests that, although the results are very close to the experimental data, the remaining mismatch between predictions and experiments is probably not coming from inadequate turbulence modelling or numerical issues, but most likely from the inlet flow rate approximation with the adopted boundary conditions. To improve the agreement more detailed μPIV measurements at the inlets should be produced and analysed.

As a final comment it is interesting to point out that similar conclusions were formulated when μPIV data was employed with DNS [22]. This proves that the most challenging issue is the proper modelling of the real operating conditions (in particular the inflow conditions) and once this is achieved, also LES is capable of describing properly the turbulent flow field inside the CIJR, at least under the operating conditions investigated in this work. It is interesting to remember here that these predictions, resulting in good agreement with experimental data, are obtained here via LES with grids that are at least ten times less refined than those used in DNS. This typically results in a reduction of the CPU time of about ten times. Last but not least, LES allows also for the simulation of liquid turbulent scalar transport and chemical reactions simply by using the same grids (and appropriate SGS mixing models) whereas DNS requires the use of much finer grids, making the DNS approach intractable for the simulation of real reacting systems.

5. Conclusions

In this work LES has been employed to simulate the flow field in a CIJR and predictions are validated against experimental data. The DNS results obtained in our previous work [22] demonstrate the importance of properly imposing the inflow boundary and therefore this approach is here extended to the LES framework. In fact, contrary to what happens with RANS, where simulations generally result in good agreement with experimental data simply employing the time averaged inlet flow rates, more details are required to run a successful LES. For the present application and under the range of operating conditions investigated the spatial discretization schemes and the SGS models were found not to be crucial for a good prediction of the turbulent behaviour of the system. However, it has been shown that the QUICK scheme, in particular at intermediate FR values performs slightly better than the HLPA. No significant differences were instead noted between the constant Smagorinsky SGS model and the dynamic model of Germano. In conclusion LES can be used instead of expensive DNS (and μPIV experiments) to obtain fast and reliable predictions, that are of particular importance when the computational model is extended to consider mixing and reactive processes. The computational model that has been validated will be extended to the simulation of turbulent precipitation processes and validated against experimental data.

Acknowledgements

The financial and technical support of Ascomp GmbH is gratefully acknowledged. The authors wish also to thank Antonello Barresi for useful suggestions and discussions.

References

[1] R.H. Müller, M. Radtke, S.A. Wissing, Solid lipid nanoparticles (SLN) and nanostructured lipid carriers (NLC) in cosmetic and dermatological preparations, Adv. Drug Delivery Rev. 54 (Suppl. 1) (2002) 131–155.
[2] E. Romanus, Magnetic nanoparticle relaxation measurement as a novel tool for in vivo diagnostics, J. Magn. Magn. Mater. 252 (2002) 387–389.
[3] R.H. Müller, Nanosuspensions for the formulation of poorly soluble drugs I. Preparation by a size-reduction technique, Int. J. Pharm. 160 (1998) 229–237.
[4] Q. Qiu Zhao, A. Boxman, U. Chowdhry, Nanotechnology in the chemical industry opportunities and challenges, J. Nanopart. Res. 5 (2003) 567–572.
[5] D. Horn, J. Rieger, Organic nanoparticles in the aqueous phase – Theory, experiment, and use, Angew. Chem. Int. Ed. 40 (2001) 4330–4361.
[6] J. Kipp, The role of solid nanoparticle technology in the parenteral delivery of poorly water-soluble drugs, Int. J. Pharm. 284 (2004) 109–122.
[7] A.J. Gesquiere, T. Uwada, T. Asahi, H. Masuhara, P.F. Barbara, Single molecule spectroscopy of organic dye nanoparticles, Nano Lett. 5 (2005) 1321–1326.
[8] A.L. Le Roy Boehm, R. Zerrouk, H. Fessi, Poly ε-caprolactone nanoparticles containing a poorly soluble pesticide: formulation and stability study, J. Microencapsul. 17 (2000) 195–205.
[9] O.V. Salata, Applications of nanoparticles in biology and medicine, J. Nanobiotechnol. 2 (2004) 177–182.
[10] Y. Liu, M.G. Olsen, R.O. Fox, Turbulence in a microscale planar confined impinging-jets reactor, Lab Chip 9 (2009) 1110–1118.
[11] F. Lince, D.L. Marchisio, A.A. Barresi, Smart mixers and reactors for the production of pharmaceutical nanoparticles: Proof of concept, Chem. Eng. Res. Des. 87 (2009) 543–549.
[12] Y. Liu, J.C. Cheng, R.K. Prud'homme, R.O. Fox, Mixing in a multi-inlet vortex mixer (MIVM) for flash nano-precipitation, Chem. Eng. Sci. 63 (2008) 2829–2842.
[13] Y. Liu, R.O. Fox, CFD predictions for chemical processing in a confined impinging-jets reactor, AIChE J. 52 (2006) 731–744.
[14] J.C. Cheng, M.G. Olsen, R.O. Fox, A microscale multi-inlet vortex nanoprecipitation reactor: Turbulence measurement and simulation, Appl. Phys. Lett. 94 (2009) 20104-1–20104-3.
[15] D.L. Marchisio, F. Omegna, A.A. Barresi, P. Bowen, Effect of mixing and other operating parameters in SolGel processes, Ind. Eng. Chem. Res. 47 (2008) 7202–7210.
[16] D.L. Marchisio, L. Rivautella, A.A. Barresi, Design and scale-up of chemical reactors for nanoparticle precipitation, AIChE J. 52 (2006) 1877–1887.
[17] F. Lince, D.L. Marchisio, A.A. Barresi, Strategies to control the particle size distribution of poly-ε-caprolactone nanoparticles for pharmaceutical applications, J. Colloid Interf. Sci. 322 (2008) 505–515.
[18] B.K. Johnson, R.K. Prud'homme, Chemical processing and micromixing in confined impinging jets, AIChE J. 49 (2003) 2264–2282.
[19] E. Gavi, D.L. Marchisio, A.A. Barresi, M.G. Olsen, R.O. Fox, Turbulent precipitation in micromixers: CFD simulation and flow field validation, Chem. Eng. Res. Des. 88 (2010) 1182–1193.
[20] H. Feng, M.G. Olsen, Y. Liu, R.O. Fox, J.C. Hill, Investigation of turbulent mixing in a confined planar-jet reactor, AIChE J. 51 (2005) 2649–2664.
[21] F. Schwertfirm, J. Gradl, H.C. Schwarzer, W. Peukert, M. Manhart, The low Reynolds number turbulent flow and mixing in a confined impinging jet reactor, Int. J. Heat Fluid Flow 28 (2007) 1429–1442.
[22] M. Icardi, E. Gavi, D.L. Marchisio, A.A. Barresi, M.G. Olsen, R.O. Fox, D. Lakehal, Investigation of the flow field in a three-dimensional Confined Impinging Jets Reactor by means of microPIV and DNS, Chem. Eng. J., submitted for publication.
[23] R.O. Fox, Computational Models for Turbulent Reacting Flows, Cambridge University Press, Cambridge, 2003.
[24] E. Gavi, Investigation of turbulent precipitation of nanoparticles in a Confined Impinging Jets Reactor, Ph.D. thesis, Politecnico di Torino, Torino, Italy, 2009.
[25] D.L. Marchisio, Large Eddy Simulation of mixing and reaction in a Confined Impinging Jets Reactor, Comput. Chem. Eng. 33 (2009) 408–420.
[26] C.D. Meinhart, S.T. Wereley, J.G. Santiago, PIV measurements of a microchannel flow, Exp. Fluids 27 (1999) 414–419.
[27] J.G. Santiago, S.T. Wereley, C.D. Meinhart, D.J. Beebe, R.J. Adrian, A particle image velocimetry system for microfluidics, Exp. Fluids 25 (1998) 316–319.
[28] H. Li, M.G. Olsen, MicroPIV measurements of turbulent flow in square microchannels with hydraulic diameters from 200 μm to 640 μm, Int. J. Heat Fluid Flow 27 (2006) 123–134.
[29] R. Lindken, M. Rossi, S. Grosse, J. Westerweel, Micro-Particle Image Velocimetry (microPIV): Recent developments, applications, and guidelines, Lab Chip 9 (2009) 2551–2567.
[30] S.B. Pope, Turbulent Flows, Cambridge University Press, Cambridge, 2000.
[31] J. Smagorinsky, General circulation experiments with the primitive equations, Mon. Weather Rev. 91 (1963) 99–164.
[32] M. Germano, U. Piomelli, P. Moin, W.H. Cabot, A dynamic subgrid-scale eddy viscosity model, Phys. Fluids A 3 (1991) 1760.
[33] Ascomp GmbH, Multi-Fluid Navier-Stokes Solver TransAT User Manual, 2009.
[34] R. Mittal, G. Iaccarino, Immersed boundary methods, Annu. Rev. Fluid Mech. 37 (2005) 239–261.
[35] C. Beckermann, H.J. Diepers, I. Steinbach, A. Karma, X. Tong, Modeling melt convection in phase-field simulations of solidification, J. Comput. Phys. 154 (1999) 468–496.

[36] J.H. Ferziger, M. Peric, Computational Methods for Fluid Dynamics, third ed., Springer-Verlag, Berlin, 2002.
[37] J. Zhu, A low-diffusive and oscillation-free convection scheme, Commun. Appl. Numer. Methods 7 (1991) 225–232.
[38] J. Denev, J. Frohlich, H. Bockhorn, F. Schwertfirm, M. Manhart, DNS and LES of scalar transport in a turbulent plane channel flow at low Reynolds number, Lect. Notes Comput. Sci. 4818 (2008) 251.
[39] B.P. Leonard, A stable and accurate convective modelling procedure based on quadratic upstream interpolation, Int. J. Mech. Sci. 16 (1976) 183–308.
[40] H. Werner, H. Wengle, Large-eddy simulation of turbulent flow over a square rib in a channel, in: Proc. 7th Symp. on Turbulent Shear Flows, Stanford University, August 21–23, 1989.
[41] E.R. Van Driest, On turbulent flow near a wall, J. Aeronaut. Sci. 23 (1956) 1007–1011.
[42] C.J. Bourdon, M.G. Olsen, a.D. Gorby, Validation of an analytical solution for depth of correlation in microscopic particle image velocimetry, Meas. Sci. Technol. 15 (2004) 318–327.
[43] M.G. Olsen, R.J. Adrian, Out-of-focus effects on particle image visibility and correlation in microscopic particle image velocimetry, Exp. Fluids 29 (2000) S166–S174.